Juan, Rongfei; Wang, Min; Li, Lanxin; Lian, Junhe; Bao, Yanping

Relationship between Inclusions and Internal Defect Spatial Distribution in Large Forging Piece for Wind Power Generation Gear

Published in:
ISIJ International

DOI:
10.2355/isijinternational.ISIJINT-2021-356

Published: 01/01/2022

Document Version
Publisher's PDF, also known as Version of record

Please cite the original version:
Juan, R., Wang, M., Li, L., Lian, J., & Bao, Y. (2022). Relationship between Inclusions and Internal Defect Spatial Distribution in Large Forging Piece for Wind Power Generation Gear. *ISIJ International*, *62*(1), 133-141. https://doi.org/10.2355/isijinternational.ISIJINT-2021-356

ISIJ International, Vol. 62 (2022), No. 1, pp. 133–141
https://doi.org/10.2355/isijinternational.ISIJINT-2021-356

Relationship between Inclusions and Internal Defect Spatial Distribution in Large Forging Piece for Wind Power Generation Gear

Rongfei JUAN,[1)] Min WANG,[1)]* Lanxin LI,[3)] Junhe LIAN[2)] and Yanping BAO[1)]

1) State Key Laboratory of Advanced Metallurgy, University of Science and Technology Beijing, Beijing, 100083 China.
2) Advanced Manufacturing and Materials, Department of Mechanical Engineering, Aalto University, Puumiehenkuja 3, Espoo, 02150 Finland.
3) Beijing National Railway Research & Design Institute of Signal & Communication Group Co. Ltd., Beijing, 100070 China.

(*Received on August 3, 2021; accepted on September 21, 2021; J-STAGE Advance published date: December 6, 2021*)

The spatial distribution of inclusions in a large forging piece is closely related to the fatigue life of gears. In this paper, the size, number, types, and distribution of inclusions in a large forging piece of gear steel used for wind-power generation have been systematically analyzed by the automatic scanning of inclusions, *in situ* analysis of inclusions, scanning electron microscopy, and energy spectrum analysis. The inclusions distribution model is established and the size of the largest inclusion in the forging piece is predicted. The distribution of the number and size of inclusions exhibits an exponential relationship. The total number of inclusions is lowest at the tooth center area, and macro-inclusions with sizes above 10 μm mainly concentrate in the tooth center, with a maximum size of 101.5 μm. The typical inclusions in forging pieces include 2.85% oxides, 80.95% sulfides and 16.2% composite inclusions of oxides and sulfides. The sulfide preferentially precipitates on the surface of oxide's core in the following order: Al_2O_3–MgO–CaO > Al_2O_3 > Al_2O_3–MgO > Al_2O_3–MgO–SiO_2–CaO > Al_2O_3–MgO–SiO_2 > Al_2O_3–SiO_2. It is helpful to change the brittle oxides into composites of oxides and sulfides to improve the fatigue life of gear steel.

KEY WORDS: gear steel; inclusions; precipitates; spatial distribution; fatigue life.

1. Introduction

Gear steel used for wind power generation is a key material for manufacturing transmission mechanical parts. Gear steel is subjected to alternating loads, such as tension, pressure, and bending, during power transmission, which often easily causes fatigue fracture at the root of the tooth. It was reported that the failure of gear steel used for wind power generation is mainly related to the inclusions, microstructure and working conditions.[1)] Non-metallic inclusions in steel, especially large brittle inclusions, would be easily transformed into fatigue sources during the service process of mechanical parts, and the maximum size of inclusions in steel could determine the fatigue limit of the steel.[2,3)]

Previous research[4,5)] has demonstrated that spinel ($MgO\cdot Al_2O_3$), calcium aluminate ($CaO\cdot Al_2O_3$), and Al_2O_3 do not have a plastic deformation ability at conventional hot rolling temperatures. And they also have a weak binding ability between the inclusions and matrix. This will lead to a large gap between the inclusions and the matrix in the process of hot rolling deformation, which will turn to a crack. Therefore, the matrix with such high-risk inclusions presented a high occurrence of fatigue fracture under the service conditions of the gear load. The inclusions have been proved to be the main factors leading to the cracks and the fatigue fracture of steel based on ultra-high-cycle fatigue tests.[6,7)] Gu *et al.*[8)] showed that the main non-deformation oxide inclusions were closely related to the crack initiation of the matrix based on the meshing stress evaluation performed between the inclusion and the matrix. The Al_2O_3 inclusions are more susceptible to defects than TiN inclusions during rolling, and the microdefects such as cracks and holes around these inclusions can cause the failure of the steel matrix.[9,10)] Zhang *et al.*[11)] analyzed the influence of the size of inclusions on the fatigue properties of steel and found that the high-cycle fatigue life and reliability of steel could be greatly improved when the sizes were controlled below 1 μm. Lu *et al.*[12,13)] also demonstrated that smaller inclusions in the steel indicated a longer fatigue life by following the S-N curve characteristics of high-strength steel. Consequently, the spatial distributions of high-risk inclusions in steel, including their sizes, types, quantities, and morphologies, play an important role in the improvement of the fatigue life of steel.

* Corresponding author: E-mail: wangmin@ustb.edu.cn

Previous researchers focused on the three-dimensional morphologies and inclusion characteristic control of gear steel,[14,15] and the spatial distribution of inclusions in forged gear steel was rarely reported. In this work, the type, quantity, size, and spatial distribution of inclusions from the tooth top to the center of the forged steel were studied using the Oxford INCA automatic inclusion analysis system. Since the fatigue failure of steel starts from the edge of large inclusions, a prediction model for the maximum inclusions in forgings is established by combining the size and number of inclusions in the forgings. The relationship between the inclusions and fatigue life of the gear steel was analyzed to provide guidance for controlling the number and size of inclusions around the gear and improve the fatigue life of the gear steel.

2. Experimental

The gear steel 18CrNiMo7-6 is produced by the following processes: electric furnace (EAF) → ladle furnace (LF) → vacuum degassing furnace (VD) → ingot cast. The main chemical composition (wt%) is C 0.16, Si 0.25, Mn 0.60, S 0.008, P 0.009, Cr 1.56, Ni 1.64, Mo 0.27, Al 0.03, Mg 0.0003 and N 0.013. The ingot was forged into a cylinder for gear processing, and the corresponding relationship between the gear and cylinder specimen is shown in **Fig. 1**. The six 21 mm × 20 mm × 15 mm rectangular block specimens were cut from the tooth top (specimens 1 and 2), the tooth root (specimens 3 and 4), and the center (specimens 5 and 6) of a 110 mm × 50 mm forged cylinder to investigate the distribution of inclusions in the diameter direction. For each specimen, four layers from 0 mm to 0.9 mm in the thickness direction were scanned at an interval of 0.3 mm between adjacent layers.

To prepare the specimens for automatic inclusion scanning, the surfaces of the specimens were polished to be mirrors with a diamond suspension after they were ground to 2 000 grit using SiC abrasive papers. An area of 13 mm × 13 mm was defined as the observation surface in the Oxford INCA system before scanning. The observation area of the metallographic specimen was automatically divided into 198 fields of view with sizes of 922 μm × 922 μm to precisely determine the characteristics of inclusions, as described in Fig. 1(c). During the scanning process, tin foil paper was adopted as a reference to identify the inclusions by contrasting the gray levels of the steel matrix, and then, the suspicious points are further determined by Energy Dispersive Spectrometer (EDS). After the scanning of each field of view, the sizes and compositions of the inclusions in each field of view are automatically counted, and the inclusions are classified into different groups based on the compositions. The spatial distribution of the inclusions in the gear steel was obtained after scanning the whole surface. The function of spacial inclusions distribution will obtain by statistic analysis. Then the large inclusion in steel will be predicted according to the inclusion distribution conditions of this type of material. Finally, ultrasonic scanning microscope will used to verify the prediction results without damaging the specimens.

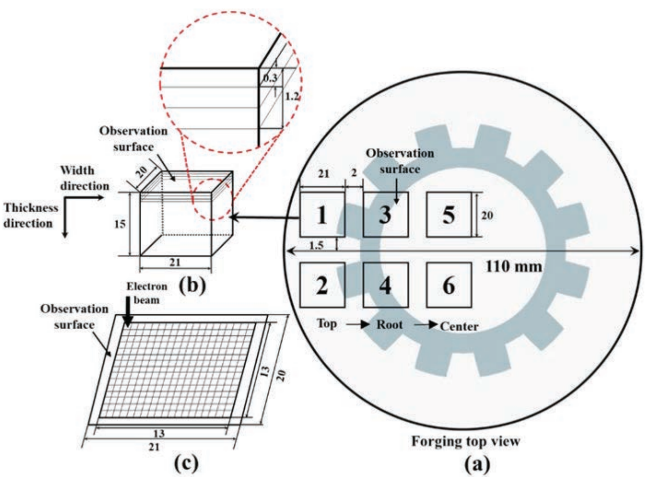

Fig. 1. Sample preparation: (a) Sampling locations on the forged gear steel, (b) sample inspection surfaces, (c) observation surface of the inclusion by automatic scanning detection. (Online version in color.)

3. Results and Discussion

3.1. Number Distribution of Inclusions in Forged Steel

A total of 24 surfaces of 6 specimens were scanned using the inclusion automatic scanning analysis. The number distribution of the different types of inclusions was summarized in **Table 1**. Although there are some differences in the number of inclusions in different layers, the distributions of inclusions in different layers seem similar. Micro-inclusions with a size below 6 μm occupy an average of more than 90% of the total number of inclusions. Macro-inclusions with sizes above 10 μm only account for 1.25% of the total number of inclusions, and the maximum size of single oxide inclusions is 101.5 μm in the tooth center of the forge.

It is assumed that the size distribution of inclusions in steel conforms to the lognormal distribution, that is, the frequency (lnd) of the logarithm of grain size conforms to the normal distribution. In the statistical process of inclusions size distribution, the distribution probability of inclusions in the plane is related to the field area and the area of inclusions, and the product of the occurrence times and area fraction of an inclusion of a certain size is taken as its distribution probability. To obtain the distribution of inclusions at different locations, the data of all inclusions were prepared to obtain a fitting curve for the number distribution of inclusions in the width directions, as shown in **Fig. 2**.

Figure 2(a) shows the relationship between the inclusion numbers and sizes, as well as the fitting curve of the inclusion number and the size distribution of the inclusions in the width direction. It can be found that the number distribution of the different sizes of inclusions presents a quasi-normal distribution, and the number of inclusions with sizes between 2 μm and 4 μm maintains the highest level in all the areas. The total number of inclusions is the lowest at the tooth center; therefore, the number of inclusions with sizes above 10 μm at the tooth center is more than that at the tooth top and the tooth root areas. At the tooth root area, the large size inclusions reach the lowest level. Figures 2(b)–2(d) demonstrates the conventional residual of the fitting curve of different areas. A low residual value reflects a good fitting curve. The abscissa and ordinate represent the regular residual value and the probability that the observation point will fall on the corresponding residual value, respectively. The drop in the vicinity of 0 accounts for 70% of the obser-

Table 1. Distribution of oxide inclusions at different locations.

Sample	Distance from the surface (mm)	Inclusion number/per 169 mm^2						Maximum size of a single inclusion (μm)
		0–2 μm	2–4 μm	4–6 μm	6–8 μm	8–10 μm	>10 μm	
1	0	741	1 110	231	23	9	5	38.75
	0.3	604	1 400	293	42	7	11	30.69
	0.6	213	600	276	65	9	11	16.1
	0.9	628	1 503	283	32	6	3	16.92
2	0	1 113	1 172	188	23	4	6	21.85
	0.3	699	1 131	145	14	3	4	29.16
	0.6	663	1 332	239	25	4	6	19.74
	0.9	699	1 274	255	21	5	2	21.55
3	0	610	1 007	181	45	11	15	33.2
	0.3	245	982	269	46	6	6	12.79
	0.6	189	977	523	123	39	25	19.9
	0.9	342	1 219	436	105	27	8	34.49
4	0	390	1 300	351	60	6	9	23.36
	0.3	164	743	520	149	26	10	13.87
	0.6	489	1 310	361	52	15	8	18.64
	0.9	569	1 210	291	40	3	4	16.5
5	0	180	293	123	49	34	26	22.94
	0.3	449	879	317	132	69	64	48.6
	0.6	307	758	283	102	56	52	37.36
	0.9	357	796	248	94	42	31	29.18
6	0	192	605	362	157	91	70	26.17
	0.3	403	607	250	108	60	93	22.67
	0.6	299	739	248	98	47	40	101.5
	0.9	355	750	232	106	39	46	21.55

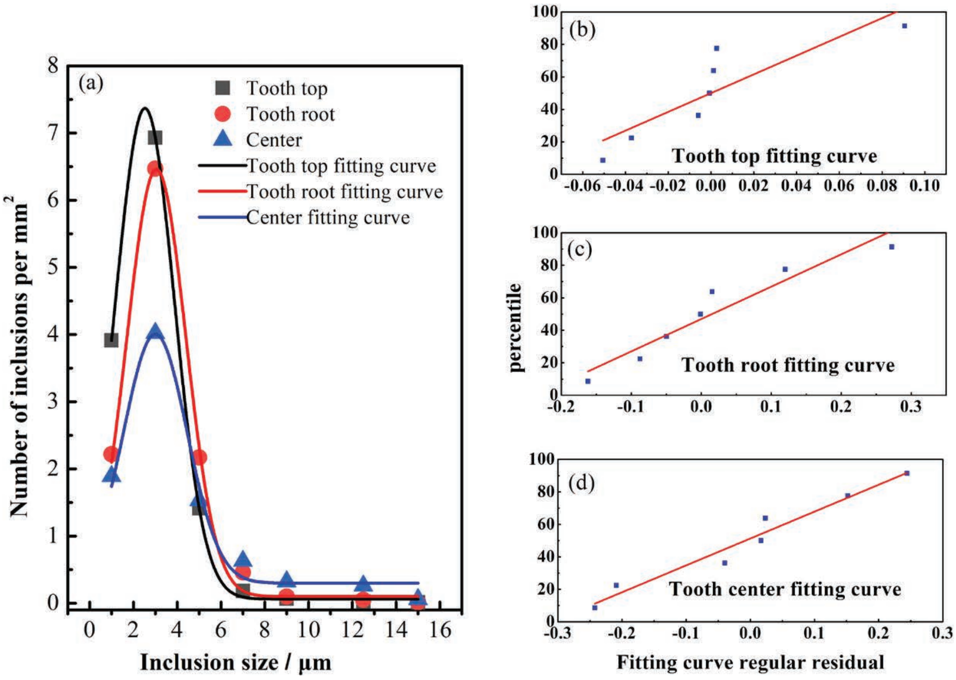

Fig. 2. The data relationship and prediction curves of the inclusion numbers and sizes, including (a) the fitting curve of the number and the size distribution of inclusions in the width direction and the regular residual of the fitting curves of the tooth top (b), root (c), and center areas (d). (Online version in color.)

vation points, and the residual verifications at different areas met the fitting evaluation conditions.

The fitting curve equation could be obtained based on Eq. (1):

$$N = N_0 + \left(\frac{A}{w\sqrt{\frac{\pi}{2}}} \times \exp\left(-2 \times \left(\frac{d - d_c}{w} \right)^2 \right) \right) \quad \text{........ (1)}$$

where N is the observed number of inclusions, and N_0 is the parameter of the number of inclusions; d is the particle size with units of μm, and d_c is the particle size parameter with units of μm; A and w are constants.

Table 2 presents the values of the fitting parameters of the inclusions at different locations. The determination coefficient R^2 value is the multiple decision coefficient of the fitting function, which is used to evaluate the fitting effect and has a range between 0 and 1. The R^2 values at each position in the table reached 0.99, and the fitted curve model was quite reasonable. As evaluated by the residual and R^2 values, the sizes and number distributions of inclusions in the width directions kept a good fitness with the curve models. Therefore, the curve models can be reliably used to determine the spatial distribution of the inclusions.

Although the number of inclusions with sizes less than 10 μm was much larger than that of the large inclusions, we emphasized the large inclusions due to their high detrimental effect to the service life of the gear. **Figure 3** shows the spatial distribution of inclusions with sizes larger than 10 μm in the forge. Here, the sizes of the different inclusions are identified by color maps. The number of large inclusions increases gradually from the tooth top to the root and ten to the center of the forge, and these inclusions are mainly complex oxide inclusions with Mg, Al, and Ca elements and a magnesium aluminate spinel ($MgO–Al_2O_3$). These kinds of inclusions mainly originate from the de-oxidation products and the reaction products of molten steel and the refractory material. The total oxygen in steel is closely related to the number of inclusions;[16] thus, it is very important to decrease the total oxygen for inclusion control. The characteristics of the inclusion distribution are as follows: the larger the size, the less uniform the distribution in the forge. Because most of the tooth top would be cut during gear machining, the inclusions located in the root of the gear are most harmful to the service life of the gear, because main loads are applied on the root position.

Table 2. Fitting parameter values at different positions.

Position	N_0	d_c	A	W	R^2
Tooth top	0.06164	2.52589	24.6924	2.6968	0.99943
Tooth root	0.1	3.05	21.47335	2.69419	0.99544
Tooth center	0.3	3	13.49708	2.90619	0.98096

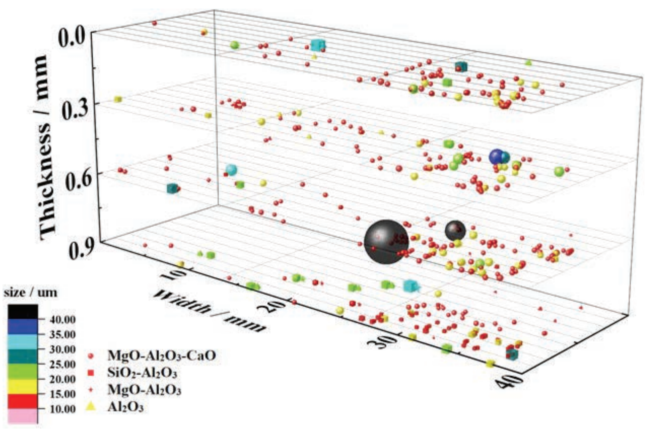

Fig. 3. Spatial distribution of inclusions with sizes above 10 μm in the forged steel. (Online version in color.)

Figure 4 shows the typical large inclusions in forged gear steel. Four types of inclusions, including Al_2O_3, $MgO–Al_2O_3$, $SiO_2–Al_2O_3$, and $MgO–Al_2O_3–CaO$, were summarized. The Al_2O_3 inclusions were mainly spherical and granular with sizes above 10 μm, as shown in Fig. 4(a). These inclusions were usually produced during the Al-killed process. The $MgO–Al_2O_3$ spinel inclusion in Fig. 4(b) presents a chain shape with a size of 50 μm. The typical $SiO_2–Al_2O_3$ inclusion, as shown in Fig. 4(c), was irregular and had a size of 30 μm, which could be related to the de-oxidation products. The shape of the $MgO–Al_2O_3–CaO$ inclusion was similar to an ellipsoid, as shown in Fig. 4(d), which was mainly due to the reaction between molten steel and the ladle lining. Here, the source of different kinds of inclusions were inferred based on the deoxidation and alloying process. For present steel, the Al and Si in the molten steel is 0.03% and 0.25% respectively. The ferro-aluminum alloy was added into the melt to remove the free oxygen during the BOF tapping, and a large of deoxidation products of Al_2O_3 are formed. During the secondary refining process, ferrosilicon alloy was added into the melt to adjust the composition. Although the Si is weaker than Al in the deoxidizing ability, the high Si content in local region during the alloying process that results in the formation of $SiO_2–Al_2O_3$. During the deep secondary refining process, the $MgO–Al_2O_3$ spinel inclusion and $MgO–Al_2O_3–CaO$ inclusions were formed due to the multiphase reaction within high basicity slag, working refractory, molten steel and deoxidation products.

3.2. Types of Inclusions in Forged Gear Steel

Figure 5 shows that the typical inclusions in the gear steel are sulfides, oxides, and their composite inclusions. The sulfides, including MnS, CaS and MnS–CaS, accounted for 80.95% of the total inclusions. The ratios of oxides and the composites of oxides and sulfides were 2.85% and 16.2%, respectively. It is known that the oxide inclusions are mainly formed during smelting processes, and most of the sulfides form more easily during the solidification and heat treatment processes. The oxides provide favorable cores for sulfide formation; thus, more than 85% of the oxides are wrapped by sulfides.

As shown in **Fig. 6**(a), six types of oxides, including Al_2O_3, $Al_2O_3–MgO$, $Al_2O_3–SiO_2$, $Al_2O_3–MgO–SiO_2$, $Al_2O_3–MgO–CaO$ and $Al_2O_3–MgO–SiO_2–CaO$, existed in the steel. The oxides have similar distributions at different layers, from 0 mm to 0.9 mm from the surface, and $Al_2O_3–MgO$ accounted for an average of 66.2% of the inclusions, which is the highest proportion of all the oxide inclusions. For the oxide inclusions with a sulfide shell shown in Fig. 6(b), $Al_2O_3–MgO–CaO–CaS$ accounts for 70.9% of the total composite inclusions of oxides and sulfides. It can be concluded from **Fig. 7** that almost all the Al_2O_3–MgO–CaO inclusions finally transformed into Al_2O_3–MgO–CaO–(MnS)–CaS due to their high sulfur capacity, which promoted the preferential precipitation of the sulfur on the surface; meanwhile, the transition rate of the Al_2O_3 and Al_2O_3–MgO inclusions reached 89.5% and 58.5%, respectively. Other oxides, including Al_2O_3–SiO_2, Al_2O_3–MgO–SiO_2 and Al_2O_3–MgO–SiO_2–CaO, maintained a very low transition rate. This indicated that the sulfides more easily precipitated on the oxide's core in the following order of priority: Al_2O_3–MgO–CaO > Al_2O_3 > Al_2O_3–MgO > Al_2O_3–MgO–SiO_2–CaO > Al_2O_3–MgO–SiO_2 > Al_2O_3–SiO_2. Combined with the calculation of mismatch degree[17] and the work done by the core, we can know that Al2O3 and MnS have relatively high mismatch degree and belong to invalid core during nucleation. Under the conditions, it is difficult to form oxide sulfide complex inclusions. The mechanism of inclusion nucleation induced by Al–O–Mg inclusions conforms to the minimum mismatch mechanism. It is proved that this type of complex inclusions

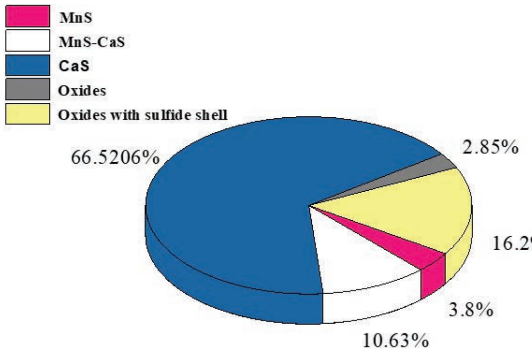

Fig. 5. Classification of different types of inclusions. (Online version in color.)

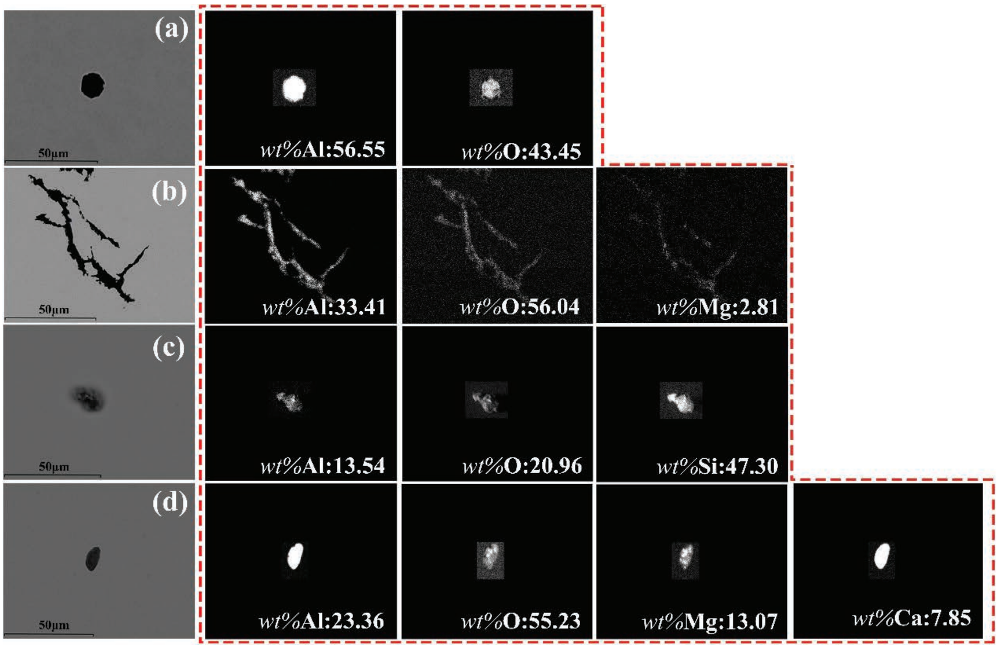

Fig. 4. Typical large inclusions in forged gear steel: (a) Al_2O_3, (b) MgO–Al_2O_3, (c) SiO_2–Al_2O_3, and (d) MgO–Al_2O_3–CaO. (Online version in color.)

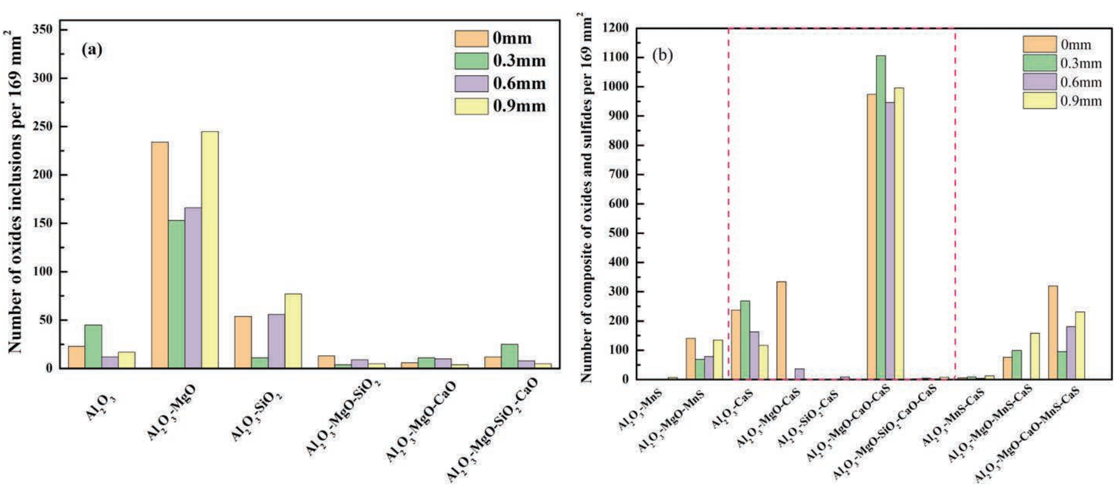

Fig. 6. Distribution of inclusions in the different layers: (a) single-phase oxides inclusions; (b) a composite of oxides and sulfides. (Online version in color.)

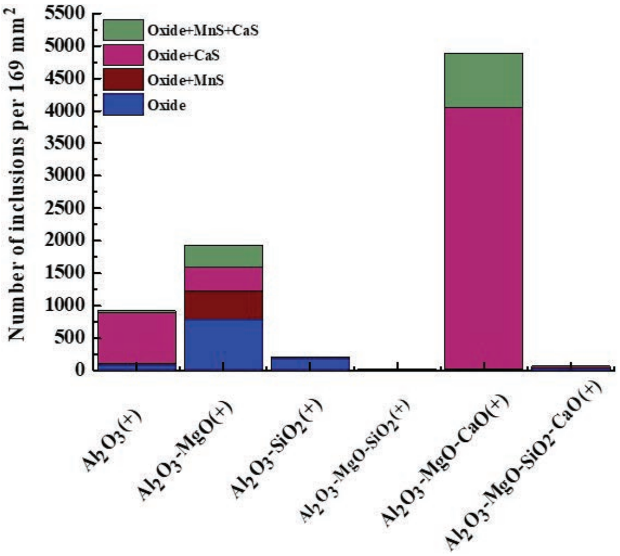

Fig. 7. Rate of different oxides transforming from single-phase oxides to composites of oxides and sulfides. (Online version in color.)

can be used as the core of effectively induced nucleation. In the Al_2O_3–SiO_2 system, only when the Al_2O_3 content is between 1% and 10%, that is, when the silicon content is relatively high, can it be used as an effective core.[18] Finally, with the addition of Ca,[19] the Mg–O–Al system becomes Mg–O–Al–Ca, which further promotes the precipitation of sulfide on the inclusions.

3.3. Size Distribution of Inclusions in Forging

Figure 8 presents a cloud map of the inclusion sizes in the width and thickness directions. The vertical axis and horizontal axis represented the thickness and width of the forged gear steel, respectively. The color map reflects the spatial distribution of different sizes of inclusions. The large inclusions marked in the green and red areas mostly appeared at the central part of the forged steel. The size of the inclusions increases gradually from the tooth top to the root. The small inclusions are more uniform than the large inclusions.

Figure 9 shows the change in the average particle diameter of the inclusions at different positions in space. The properties of the oxide inclusions and sulfide inclusions in the steel were quite different,[20] and the distributions of the inclusions in the forged steel greatly affected the fatigue life. The results in Fig. 9(a) show that the average size of the sulfide inclusions from the tooth top to the center has a tendency to grow, and it reached a maximum in the tooth root area. Sulfide inclusions possess a very good deformability, which could eliminate the hazards of the high hardness and brittleness of the oxides by wrapping the oxides, improving the fatigue life of the gear steel. Figure 9(b) presents the change in the average particle size of the oxide inclusions at different positions in space. The oxide inclusion in the central portion is relatively larger than that in the tooth top and root, which was consistent with the particle size distribution of the inclusions in the cloud diagram. The large size of the inclusions in the forged pieces were dominated by the oxide's inclusions. Therefore, the control of the oxide's inclusions, especially large oxide inclusions, is the key to the improvement of the fatigue life of gear steel.

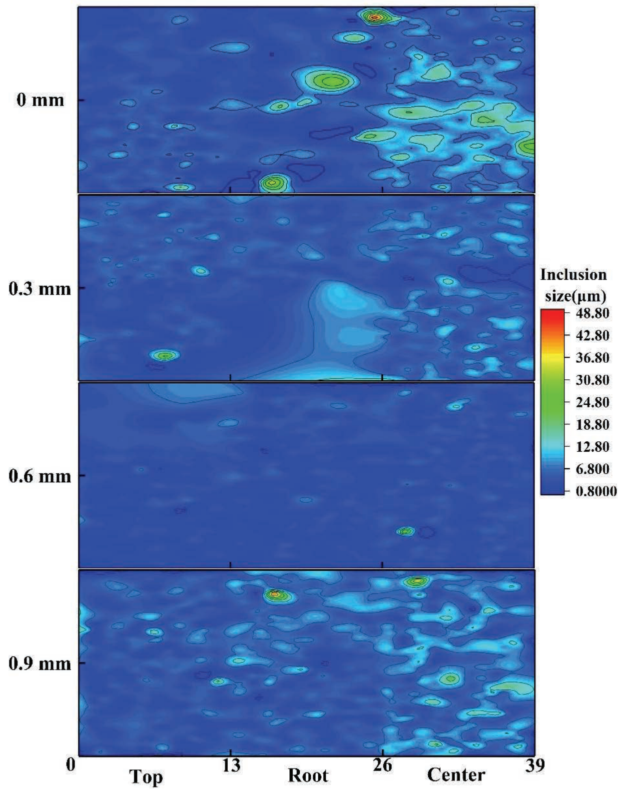

Fig. 8. Cloud map of the size distribution of inclusions in forged gear steel. (Online version in color.)

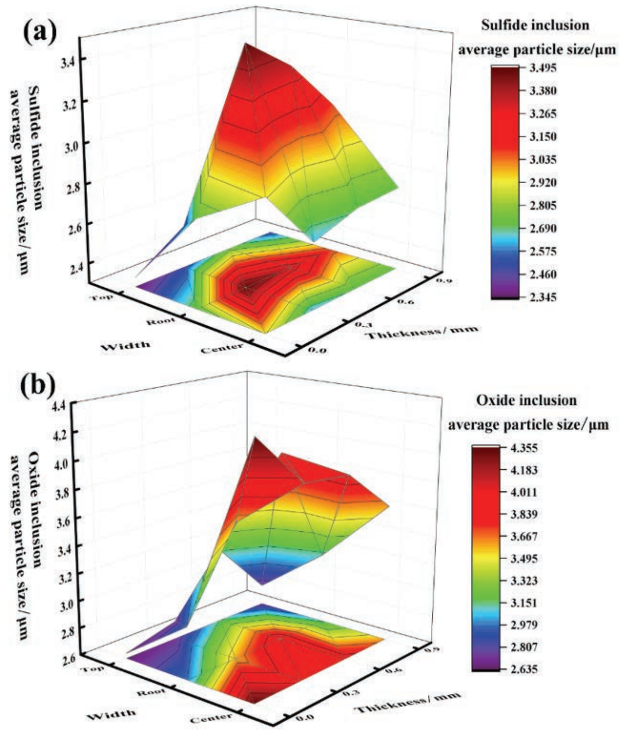

Fig. 9. Average particle size of the oxide and sulfide inclusions in space: (a) sulfide inclusions, (b) oxide inclusions. (Online version in color.)

3.4. Largest Extreme Value Distribution

According to the data of the number, size and type of inclusions in the forgings, the model of the possible large inclusions in the large volume steel is established by using the information of the inclusions in the limited field of view.[21] It can be used to avoid the defect that the instrument is not accurate enough to measure very small inclusions. The largest extreme value distribution (LEVD) is estimating the distribution of the maximum value according to some independent data of a certain number of random fields.[22] There only are the maximum inclusions in the selected fields should be measured.

The inclusions in the 6 rectangular sample blocks taken at different positions were taken as the sample population, and the inclusions in the section of each rectangular block in the direction of thickness were regarded as subsamples. Then the maximum particle size of inclusions in each sample (X1, X2...Xn) conforms to the distribution of the Gumbel[23] approximation function (as shown in the **Fig. 10**, the area of each sample is S_0). The maximum particle sizes of 4 sections in the direction of thickness of 8 samples were estimated by LEVD statistics method and the maximum inclusion particle sizes under the cumulative distribution of different Gumbel distributions were calculated. Generally, the larger the sample is, the predicted value of the extreme value distribution will be.

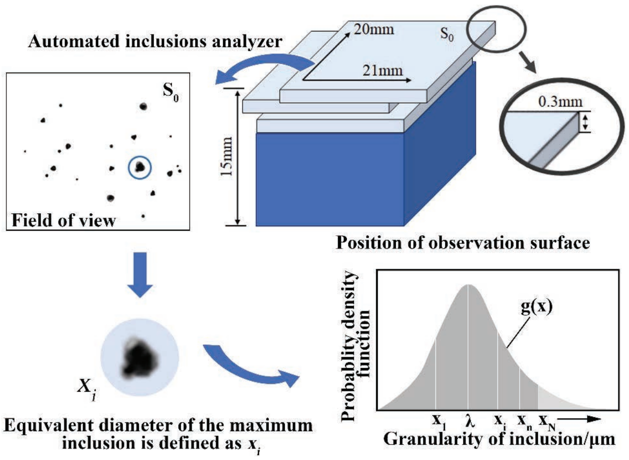

Fig. 10. Schematic diagram of sampling observation by statistical extremum method. (Online version in color.)

The LEVD has the following probability density function[24]

$$g(x)=\frac{1}{\delta}\cdot\exp\left\{-\left[\left(\frac{x-\lambda}{\delta}\right)+\exp\left(-\frac{x-\lambda}{\delta}\right)\right]\right\} \quad \text{...... (2)}$$

and cumulative probability function

$$G(x)=\exp\left\{-\exp\left[-\frac{(x-\lambda)}{\delta}\right]\right\} \quad \text{................ (3)}$$

λ and δ are referred to as the location and scale parameter respectively.

Define a standard field of view and statistic the equivalent diameter (x) of the maximum inclusion in each standard field of view. The cumulative probability of the i-th defect size not greater than x_i is:

$$G(x_i)=\frac{i}{(N+1)} \quad \text{............................ (4)}$$

After the estimated value ($\hat{\lambda}$, $\hat{\delta}$) of parameter λ and δ is obtained, the maximum inclusion size value x_{max} can be calculated under probability $G(x)$ by Eq. (5):

$$x_{\max}=\hat{\delta}\cdot[-\ln(G(x))]+\hat{\lambda} \quad \text{..................... (5)}$$

Define y as the standardized variable:

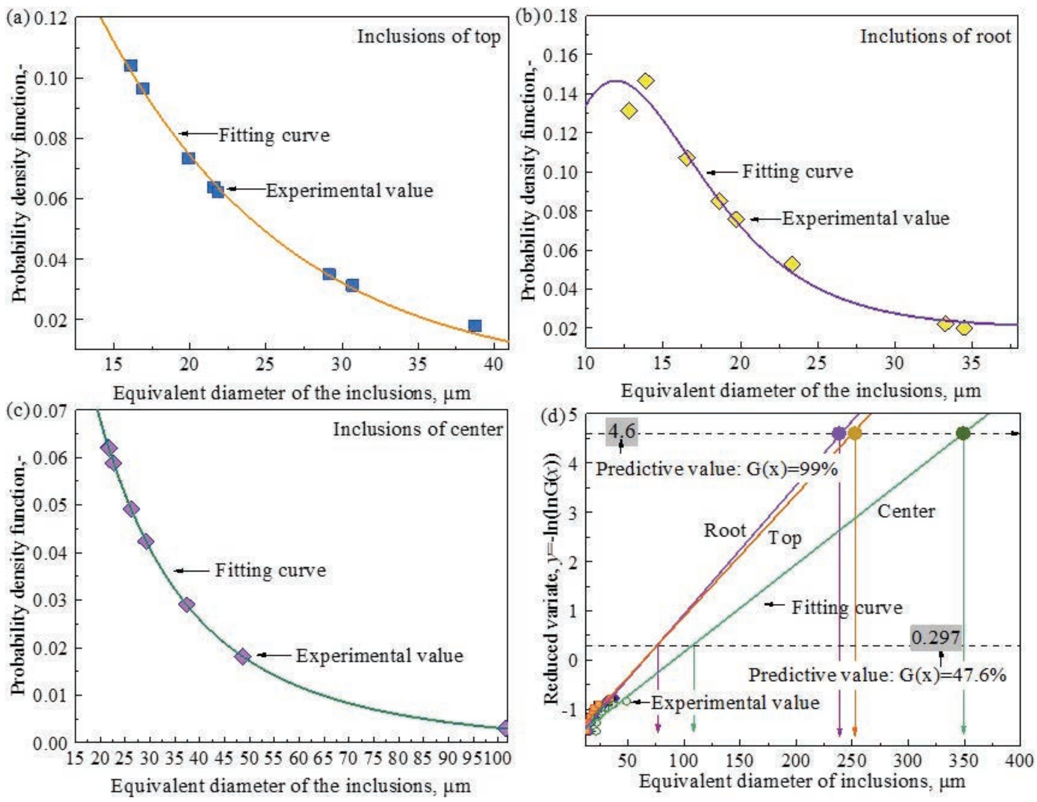

Fig. 11. Probability density function of inclusions distribution at different locations (a–c) and predictive value of maximum inclusion in LEVD method (d). (Online version in color.)

$$y = -\ln(-\ln G(x)) \quad (6)$$

The λ and δ of the formula can be calculated from the measured value of the maximum particle size of each sub-sample and the corresponding y. And y is given by the corresponding $G(x)$ in terms of Eq. (6). Combined with the Eq. (5), the maximum particle size(x_{max}) of the whole population can be obtained.

The drawing results are shown in **Fig. 11**. According to the analysis results, when the cumulative distribution function $G(x)$ is 99%, the predicted largest inclusion in the tooth top is about 250 μm, the predicted largest inclusion in the tooth root is about 240 μm and the inclusion in the tooth center is about 350 μm. Therefore, under the condition of sufficient data, the maximum value of inclusion in the material with a specified volume can be inferred by LEVD analysis method. The more samples, the more accurate the prediction will be.[25] With the support of certain data conditions, the model can play a role in the pre-evaluation of continuous production of large steel quality in the actual production process.[26]

A rectangular sample block with a surface of 200 mm × 180 mm was arbitrarily taken from the sample and put into an ultrasonic immersion flaw detection scanning microscope. A 50 MHz probe was used to detect the defects inside the sample. The inclusions in the depth range of 1 mm and 1.5 mm below the surface were detected, and the inclusions predicted by the extreme value distribution analysis were verified. Sample preparation and detection process are shown in **Fig. 12**. The longitudinal scanning range of the probe is ± 0.5 mm, and the volume is 18 000 mm^2. The cumulative distribution function G(x) at this volume is

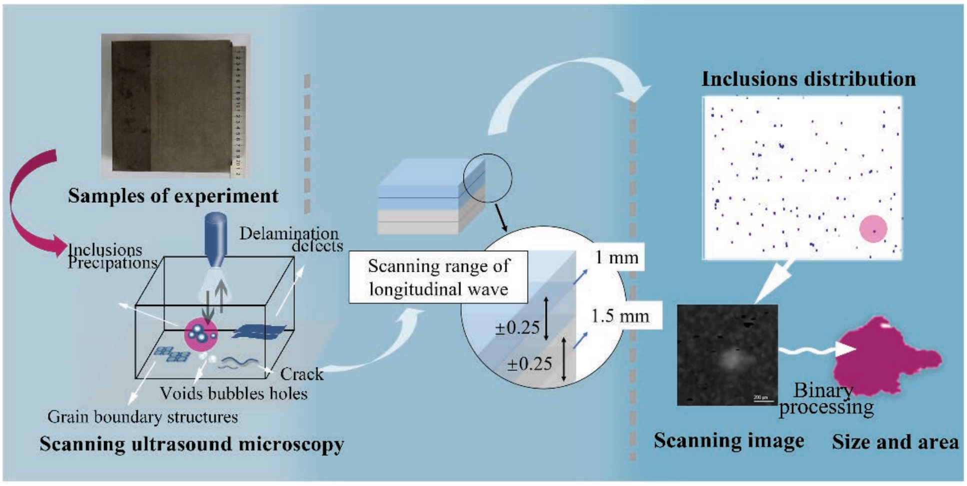

Fig. 12. The process of sample preparation and experimental detection. (Online version in color.)

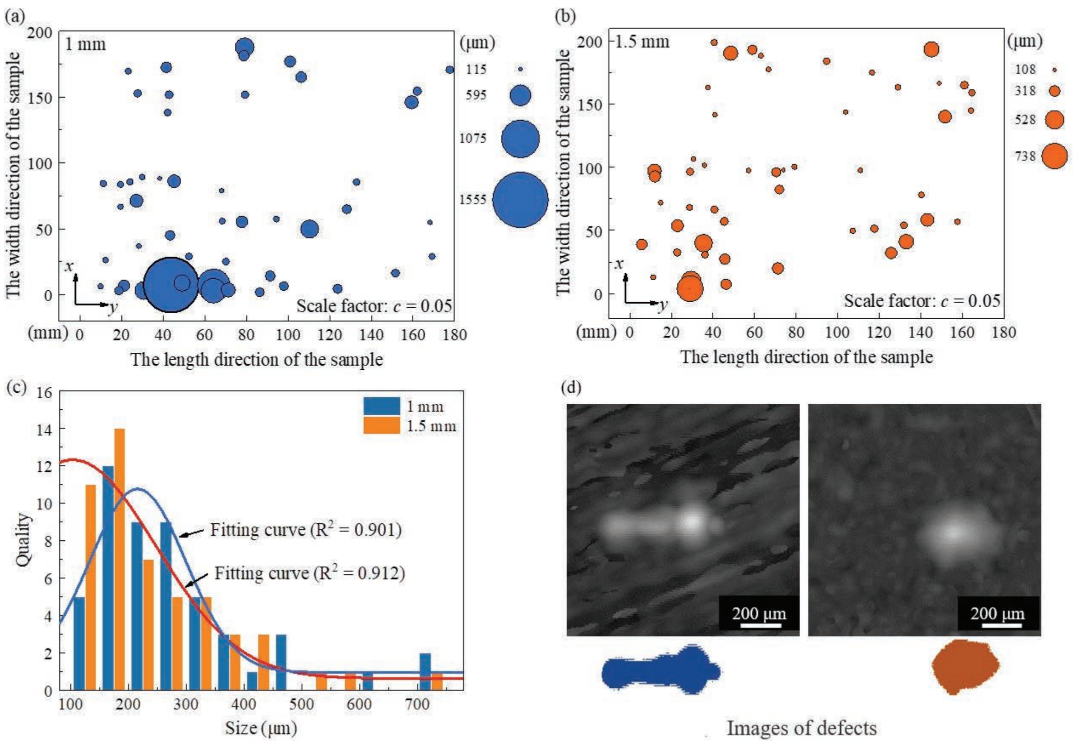

Fig. 13. The distribution of inclusions at 1 mm (a) depth and 1.5 mm (b) depth, as well as the statistics of the quantity (c) and images of the maximum inclusions (d). (Online version in color.)

47.6%, and the maximum value of inclusions' size in this volume range is estimated to be about 110 μm according to the extreme value distribution analysis method, which is also given in Fig. 11(d) above.

The size and distribution of inclusions within the range of 1 mm and 1.5 mm are shown in **Figs. 13**(a) and 13(b), respectively. It can be seen that the inclusions at different depths are mainly similar in distribution, and the inclusions near larger inclusions are also densely distributed. Figure 13(c) shows the statistical histogram of inclusion distribution on the two depth interfaces, which all conform to normal distribution after fitting the distribution rule. The area and equivalent diameter of the large inclusions on the two surfaces were obtained by fine surface scanning. The images of the maximum inclusions on the two interfaces are shown in Fig. 13(d), respectively. The maximum inclusions on the 1 mm and 1.5 mm interfaces are calculated to be 156 555 μm^2 and 44 126 μm^2.

In summary, the largest inclusion in this volume range is the largest inclusion on the 1 mm interface, and its equivalent diameter is 395.7 μm, which is 3.6 times of the predicted value. Because the images of ultrasonic microscope scan are gotten from the echo of the outermost contour of the inclusion, while the automatic scanning of the inclusion is the original metallographic scanning electron microscope imaging, to get the cross-sectional area of the inclusion. Typically, ultrasonic scanning microscopes produce inclusions three to four times the size of electron scanning microscopes,[27] so the results are valid.

4. Conclusions

The spatial distributions of inclusions in terms of the types, quantities, sizes, and morphologies of the inclusions along the tooth top, tooth root and center of a forging piece were investigated using an inclusion automatic scanning analyzer. The relationship between the inclusions and fatigue life of the gear steel was analyzed to provide guidance for controlling the inclusions and improving the fatigue life of the gear steel. The main conclusions are as follows:

(1) The typical inclusions in the forging piece include 2.85% oxides, 80.95% sulfides and 16.2% oxide-sulfide complex inclusions. For the composite inclusions of oxides and sulfides, the sulfides preferentially precipitate on the surface of oxide's core in the following order: Al_2O_3–MgO–CaO > Al_2O_3 > Al_2O_3–MgO > Al_2O_3–MgO–SiO_2–CaO > Al_2O_3–MgO–SiO_2 > Al_2O_3–SiO_2.

(2) The number distribution of different sizes of inclusions in the forging piece presents a quasi-normal distribution with a peak in the range from 2 μm to 4 μm. The total number of inclusions was lower at the tooth center than at the tooth top and tooth root areas, and the macro-inclusions with sizes above 10 μm were mainly concentrated in the tooth center area.

(3) The relationship between the inclusion distribution and the number and size of inclusions agrees with the formula $N = N_0 + \left(\frac{A}{w\sqrt{\frac{\pi}{2}}} \times \exp\left(-2 \times \left(\frac{d - d_c}{w} \right)^2 \right) \right)$. The multiple determination coefficient of the fitting function (R^2) reached 0.99.

(4) The size threshold should be controlled below 10 μm to reach 10^9 fatigue cycles under a 900 MPa working load.

(5) The maximum value of inclusions in each sample of the forgings follows the distribution of Gumbel function. The size of the largest inclusions in the sample was predicted by LEVD analysis. The predicted results showed that the inclusion volume at the top, root and center of the tooth was about 250 μm, 240 μm and 350 μm, respectively. Ultrasonic scanning microscope was used to calculate the inclusions inside the sample and verify the accuracy of the results, which proved to be valid.

Acknowledgements

This research is supported by the State Key Laboratory of Advanced Metallurgy Foundation (No. 41618019) and the National Key R&D Program of China (2016YFB0300102). The authors express their heartfelt thanks and gratitude to it.

REFERENCES

1) U. Karr, R. Schuller, M. Fitzka, B. Schönbauer, D. Tran, B. Pennings and H. Mayer: *J. Mater. Sci.*, **52** (2017), No. 10, 5954.
2) B. H. Choi and S. H. Song: *J. Mater. Sci.*, **40** (2005), No. 20, 5427.
3) S. Beretta and Y. Murakami: *Metall. Mater. Trans. B*, **32** (2001), No. 3, 517.
4) X. Li, Y. P. Bao and M. Wang: *Trans. Indian Inst. Met.*, **71** (2018), No. 5, 1067.
5) C. Gu, J. Lian, Y. P. Bao and S. Münstermann: *Mater. Sci. Eng. A*, **751** (2019), 133.
6) G. Donzella, M. Faccoli, A. Mazzù, C. Petrogalli and H. Desimone: *Eng. Fract. Mech.*, **78** (2011), No. 16, 2761.
7) L. Dimitrov, D. Michalopoulos, C. A. Apostolopoulos and T. D. Neshkov: *J. Mater. Eng. Perform.*, **18** (2009), No. 7, 939.
8) C. Gu, Y. P. Bao, P. Gan, M. Wang and J. S. He: *Int. J. Miner. Metall. Mater.*, **25** (2018), No. 6, 623.
9) R. Wang, Y. P. Bao, Z. J. Yan, D. Z. Li and Y. Kang: *Int. J. Miner. Metall. Mater.*, **26** (2019), No. 2, 178.
10) F. M. Al-Abbasi and J. A. Nemes: *Int. J. Mech. Sci.*, **45** (2003), No. 9, 1449.
11) J. Zhang, S. X. Li, Z. G. Yang, G. Y. Li, W. J. Hui and Y. Q. Weng: *Int. J. Fatigue*, **29** (2007), No. 4, 765.
12) L. T. Lu, J. W. Zhang and K. Shiozawa: *Fatigue Fract. Eng. Mater. Struct.*, **32** (2009), No. 8, 647.
13) Z. Sun, W. Li, H. Deng and Z. Zhang: *Eng. Fail. Anal.*, **59** (2016), 28.
14) M. Wang, W. Xiao, P. Gan, C. Gu and Y. P. Bao: *Metals*, **10** (2020), No. 2, 201.
15) Y. S. Hong, Z. Q. Lei, C. Q. Sun and A. G. Zhao: *Int. J. Fatigue*, **58** (2014), 144.
16) C. Gu, W. Q. Liu, J. H. Lian and Y. P. Bao: *Int. J. Miner. Metall. Mater.*, **28** (2021), No. 5, 826.
17) A. M. Guo, S. R. Li, J. Guo, P. H. Li, Q. F. Ding, K. M. Wu and X. L. He: *Mater. Charact.*, **59** (2008), 134.
18) T. Nishizawa, I. Ohnuma and K. Ishida: *J. Phase Equilib.*, **22** (2001), 269.
19) Z. Liu, B. Song and J. Mao: *Ironmaking Steelmaking*, **48** (2021), 1115.
20) K. Hashimoto, K. Hiraoka, K. Kida and E. Costa Santos: *Mater. Sci. Technol.*, **28** (2012), No. 1, 39.
21) S. Beretta: *Int. J. Fatigue*, **86** (2021), 1.
22) S. Beretta and Y. Murakami: *Fatigue Fract. Eng. Mater. Struct.*, **21** (1998), 1049.
23) X. Pan and J. Yang: *Metals*, **10** (2020), 637.
24) M. Charras-Garrido and P. Lezaud: *J. Soc. Fr. Stat.*, **154** (2013), No. 2, 66.
25) S. Guan, X. Wang, L. Hua and L. Li: *Appl. Acoust.*, **173** (2021), 107714.
26) J. Takahashi: *ISIJ Int.*, **49** (2009), 1030.
27) R. Juan, M. Wang, J. Lian, C. Gu, L. Li and Y. Bao: *Materials*, **14** (2021), 1475.